nanomanufacturing

MDPI

Article

Electronic, Structural, Optical, and Electrical Properties of $CsPbX_3$ Powders (X = Cl, Br, and I) Prepared Using a Surfactant-Free Hydrothermal Approach

Carlos Echeverría-Arrondo [1], Agustin O. Alvarez [1], Sofia Masi [1], Francisco Fabregat-Santiago [1] and Felipe A. La Porta [1,2,3,*]

[1] Institute of Advanced Materials (INAM), Universitat Jaume I, Av. Sos Baynat, s/n, 12006 Castellón, Spain
[2] Nanotechnology and Computational Chemistry Laboratory (NANOQC), Federal Technological University of Paraná, Avenida dos Pioneiros 3131, Londrina 86036-370, PR, Brazil
[3] Post-Graduation Program in Chemistry, State University of Londrina, Londrina 86057-970, PR, Brazil
* Correspondence: felipelaporta@utfpr.edu.br

Abstract: Recently, several strategies have been adopted for the cesium lead halide, $CsPbX_3$ (X = Cl, Br, and/or I), crystal growth with a perovskite-type structure, paving the way for the further development of innovative optoelectronic and photovoltaic applications. The optoelectronic properties of advanced materials are controlled, in principle, by effects of morphology, particle size, structure, and composition, as well as imperfections in these parameters. Herein, we report a detailed investigation, using theoretical and experimental approaches to evaluate the structural, electronic, optical, and electrical properties of $CsPbX_3$ microcrystals. The microcrystals are synthesized successfully using the hydrothermal method without surfactants. This synthetic approach also offers an easy upscaling for perovskite-related material synthesis from low-cost precursors. Lastly, in this direction, we believe that deeper mechanistic studies, based on the synergy between theory and practice, can guide the discovery and development of new advanced materials with highly tailored properties for applications in optoelectronic devices, as well as other emergent technologies.

Keywords: hydrothermal processing; DFT calculations; cesium lead halide perovskites; crystals

Citation: Echeverría-Arrondo, C.; Alvarez, A.O.; Masi, S.; Fabregat-Santiago, F.; Porta, F.A.L. Electronic, Structural, Optical, and Electrical Properties of $CsPbX_3$ Powders (X = Cl, Br, and I) Prepared Using a Surfactant-Free Hydrothermal Approach. *Nanomanufacturing* **2023**, *3*, 217–227. https://doi.org/10.3390/nanomanufacturing3020013

Academic Editor: Riccardo Frisenda

Received: 19 January 2023
Revised: 3 May 2023
Accepted: 5 May 2023
Published: 19 May 2023

Correction Statement: This article has been republished with a minor change. The change does not affect the scientific content of the article and further details are available within the backmatter of the website version of this article.

1. Introduction

Due to their extraordinary physical properties, lead halide perovskites have attracted noteworthy interest in emerging technologies (photovoltaic, sensor, optoelectronic, etc.) [1–4]. Notably, lead halide perovskite structures are found in related compounds with the general formula $APbX_3$, usually consisting of a ternary combination of corner-sharing $[PbX_6]$ polyhedral clusters in the lattice with an organic or inorganic monovalent cation A, such as methylammonium (MA), formamidinium (FA), or cesium (Cs), with the X site being primarily a monovalent halide (i.e., Cl, Br, I, or a combination thereof) anion [3]. It is well known that $APbX_3$-related compounds can adopt four phases (a-cubic, b-tetragonal, and g- and d-orthorhombic) depending on the tilt and rotation of the $[PbX_6]$ polyhedral clusters in the lattice [4–7]. For this reason, the formation mechanisms of the most likely crystal structure of lead halide perovskites have been widely studied in the literature from the perspective of the Goldschmidt tolerance factor, t, defined as t = (rA + rX)/[sqrt(2)(rB + rX)], where rA, rB, and rX are the ionic radii of the individual A, B, and X species, respectively [7]. Hence, according to this empirical relation, when t ranges from 0.7 to 1, stable lead halide perovskites can generally be formed [3,8,9].

Such materials have a high power conversion efficiency (PCE) with a record of 25.8% (certified 25.5%), which has been achieved over the last decade [10]. Despite this significant PCE result, however, the stability of $APbX_3$-based devices is still weak with regard to

well-established photovoltaic technologies [9–12]. It has also been reported that the metallization method of perovskite solar cells significantly impacts device efficiency (i.e., mainly due to the well-known plasmonic effect) [13,14]. Overall, the addition of nanoscale additives in the form of metallic nanoparticles is an important strategy for enhancing the optoelectronic properties and performance/durability of perovskite-based solar cells, as they can act as nucleation sites for the growth of larger perovskite crystals [13–16]. On the other hand, recent studies have reported that, among these materials, cesium lead halide (e.g., $CsPbCl_3$, $CsPbBr_3$, and $CsPbI_3$) crystals with a perovskite-type structure have higher chemical stability and are far less soluble (in the significant solvents) compared with organic/inorganic (hybrid) compounds [2,17–19]. Indeed, diverse synthetic strategies have widely been adopted to obtain ternary Cs–Pb–X compounds, including solid-state reaction [20], coprecipitation [21], hot injection [2], Bridgman growth [22], sol–gel [23], and hydrothermal [24–29]. Among them, hydrothermal methods (Scheme 1) are a promising approach to the large-scale production of these materials with a low-cost and low-temperature process [24–28]. Although this synthetic approach can be considered highly innovative, mainly thanks to the leading role in obtaining a considerable variety of metastable phases with attractive and entirely new properties, interesting in the technological field [24–29], it should be noted that the use of hydrothermal methods for the preparation of lead halide perovskites has been neglected in the literature, when compared to the other methods mentioned. However, because of the current need to obtain perovskite powders from low-cost precursors for large-scale device manufacturing, applied in numerous industrial and scientific research possibilities in the field of energy, we believe that using this synthetic approach can be quite enjoyable for this purpose in the future [30,31].

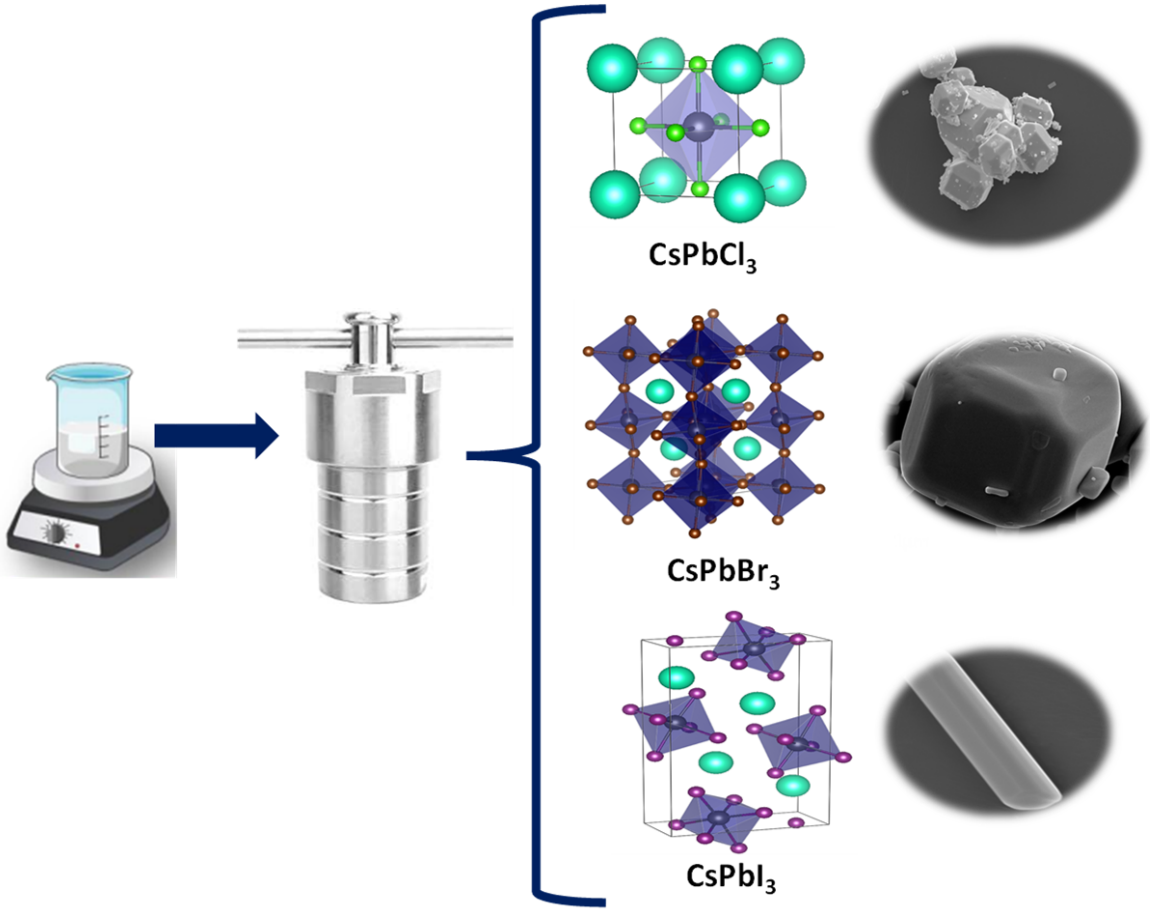

Scheme 1. Hydrothermal synthesis of $CsPbX_3$ crystals from precursor dispersion.

For instance, Kayalvizhi et al. [27] reported the stoichiometric control of ternary Cs–Pb–Br crystals based on the Cs/Pb ratios used in hydrothermal synthesis. It is important to emphasize that the solvent usually used in and after perovskite synthesis can change the stoichiometry, as previously discussed in [29]. For this reason, many recent studies have used mechanochemical methods for the production of large amounts of perovskite crystals, which is a well-known synthetic strategy for the preparation of solvent-free materials [32–34]. Despite this, it is important to highlight here that the hydrothermal method makes it possible to easy obtain of huge variety of materials with a high level of purity and unique properties, which most of the time cannot be achieved via other synthetic methods [35,36]. Hence, the hydrothermal method is an interesting choice to meet the development of a surfactant-free lead halide perovskites crystals synthesis with practical applications, with the advantage of easy tailoring desired parameters based on the tuning of the synthesis conditions and, in turn, the final material properties, thus enlarging the window of applications [24–29,31].

In this paper, we report a combined experimental/computational investigation on the electronic, structural, optical, and electrical features of $CsPbX_3$ microcrystals (X = Cl, Br, and I) synthesized successfully using the surfactant-free hydrothermal method. To complement the experiments, we performed periodic density functional theory (DFT) calculations for a better understanding of the experimental data. Of course, computational design methods are at the forefront of knowledge and have a pivotal role in elucidating the electronic structure of several advanced materials, i.e., contributing to accelerating the development of better materials. Our work highlights the importance of controlling and understanding the physical properties, and our approach is relevant to address the issue of the structural and electronic disorder degree in crystalline materials [37].

2. Materials and Methods

2.1. Materials and Hydrothermal Synthesis of $CsPbX_3$ Powders

All reagents were purchased from Sigma-Aldrich, including lead carbonate ($PbCO_3$, 98%), cesium carbonate (Cs_2CO_3, 99%), hydrogen chloride (HCl, 36 wt.%), hydrogen bromide (HBr, 48 wt.%), and hydrogen iodide (HI, 47 wt.%), and they were used without further purification. $CsPbX_3$ powders were synthesized according to the hydrothermal method using stoichiometric amounts of $PbCO_3$ and Cs_2CO_3 in a 1:1 molar ratio that were dissolved in 15 mL of 6 M haloid acid solution (HCl, HBr, or HI, respectively) under constant stirring for approximately 10 min. In sequence, the mixture reaction was transferred into a Teflon autoclave that was properly sealed and placed inside a muffle furnace. For all cases, the hydrothermal process was performed free of any template and/or surfactants using a heating rate of 10 °C·min^{-1} at 140 °C for 2 h.

2.2. Characterization

The as-prepared powders were characterized using a Raman spectrometer model NRS-3100 (JASCO) with He–Ne and Argon ion lasers used for excitation at 633 nm. X-ray powder diffraction measurements in a 2θ range from 10° to 70° at 0.01°·min^{-1} using an X-ray diffractometer (D8 Advance, Bruker-AXS) with Cu K_α radiation (λ = 1.5406 Å) are shown in the Figure S1 (in Supplementary Materials). The morphology of the prepared CsPbX3 powders was analyzed using field-emission scanning electron microscopy (SEM, JEOL 7001F). In this case, the optical properties were then analyzed using UV/Vis absorption spectroscopy with a Cary 300 Bio spectrophotometer operating in diffuse reflection mode. For measurement of the electrical response, polycrystalline pellets (with a diameter of 13.0 cm and a thickness of 4.0 mm) were prepared from the powders by cold-pressing at approximately 5 tons for 15 min, and then dried at 80 °C for 180 min. Subsequently, both sides of the pelletized samples were coated with a gold (Au) layer (approximately 100 nm thick), which was thermally evaporated at a rate of 0.8 A·s^{-1} in an ultrahigh vacuum chamber. The capacitance and impedance spectroscopy measurements of the $CsPbX_3$ pellet coated with Au were acquired using a Solartron 1260A Impedance/Gain-Phase Analyzer.

2.3. Computational Method and Models

The theoretical description of $CsPbCl_3$, $CsPbBr_3$, and $CsPbI_3$ materials is based on computations performed with Quantum ESPRESSO, a density functional theory (DFT) code [38]. The ground-state electronic properties were obtained in two steps. First, we relaxed the atomic positions in the supercell until the forces on the individual nuclei became smaller than 0.001 Ry/Bohr (0.026 eV/A). We used spin polarization, the Optimized Norm-Conserving Vanderbilt pseudopotentials (SG15 ONCV database [39,40]), a plane-wave cutoff energy of 60 Ry, and a Monkhorst–Pack k-point grid over the first Brillouin zone ($13 \times 13 \times 13$ for $CsPbCl_3$, $6 \times 4 \times 6$ for $CsPbBr_3$, and $4 \times 8 \times 3$ for $CsPbI_3$). Second, we computed the electronic parameters of the relaxed structures including spin–orbit interactions for a coarser k-point grid ($9 \times 9 \times 9$ for $CsPbCl_3$, $4 \times 3 \times 4$ for $CsPbBr_3$, and $3 \times 6 \times 2$ for $CsPbI_3$).

We also investigated $CsPbX_3$ crystals with halide vacancy defects. The computed defective supercells were composed of 134 atoms in the case of $CsPbCl_3$ ($3 \times 3 \times 3$ unit cells), 159 atoms in the case of $CsPbBr_3$ ($2 \times 2 \times 2$ unit cells), and 159 atoms in the case of $CsPbI_3$ ($2 \times 4 \times 1$ unit cells). Since one anion was missing from the studied crystal (either Cl, Br, or I), the considered vacancy concentration was approximately 1%. This anion yielded a color center at the vacancy site and one Bohr magneton per unit cell. All these spin-polarized DFT calculations were run on the Γ point without including spin–orbit interactions.

We also calculated the activation energy for halide migration inside $CsPbCl_3$, $CsPbBr_3$, and $CsPbI_3$ materials. To simulate the diffusion process, the referred ion was displaced in a series of small regular steps within the crystal. In the case of $CsPbCl_3$, the supercell contained 39 atoms in eight unit cells, and its dimensions were 11.46/11.46/11.46 Å; in the case of CsPbBr3, 19 atoms were in a single unit cell with size 8.54/11.93/8.23 Å; in the case of $CsPbI_3$, 39 atoms were in two unit cells with size 10.75/9.77/18.18 Å. The total energies were calculated for every position of the migrating ion along the diffusion path using the Quantum ESPRESSO code [38], Optimized Norm-Conserving Vanderbilt pseudopotentials, a $2 \times 2 \times 2$ k-point grid, and a kinetic energy cutoff of 70 Ry. For initial and final steps, we relaxed the positions of all the atoms in the cells; however, for the intermediate steps, we relaxed all but the position of the migrating ion, which was kept fixed.

3. Results and Discussion

Figure 1A–C show the micro-Raman spectra obtained at room temperature for the $CsPbX_3$ crystals synthesized using the hydrothermal method at 140 °C. We experimentally observed four Raman-active modes for both $CsPbCl_3$ (at approximately 78, 160, 300, and 490 cm^{-1}) and $CsPbBr_3$ (at approximately 76, 128, 152, and 308 cm^{-1}) crystals, as shown in Figure 1A,B, while the pure $CsPbI_3$ crystals exhibited Raman-active modes at 85 and 375 cm^{-1}. These Raman data are in good agreement with those reported in the literature [41,42]. The insets of Figure 1A–C show a schematic representation of the unit cells, cubic phase for $CsPbCl_3$, and orthorhombic phase in both $CsPbBr_3$ and δ-$CsPbI_3$. The structural parameters of $CsPbX_3$ crystals were obtained from DFT calculations (for $CsPbCl_3$, a = 5.73 Å; for $CsPbBr_3$ a = 8.54 Å, b = 11.93 Å, and c = 8.23 Å; for δ-$CsPbI_3$, a = 10.75 Å, b = 4.89 Å, and c = 18.18 Å), which are in accordance with the literature values related to the same compounds but synthesized using different methods [22,43–45]. The calculated Pb–anion bond lengths and bond angles (Pb–X–Pb) in $CsPbX_3$ are also in accordance with the literature [22,43–45].

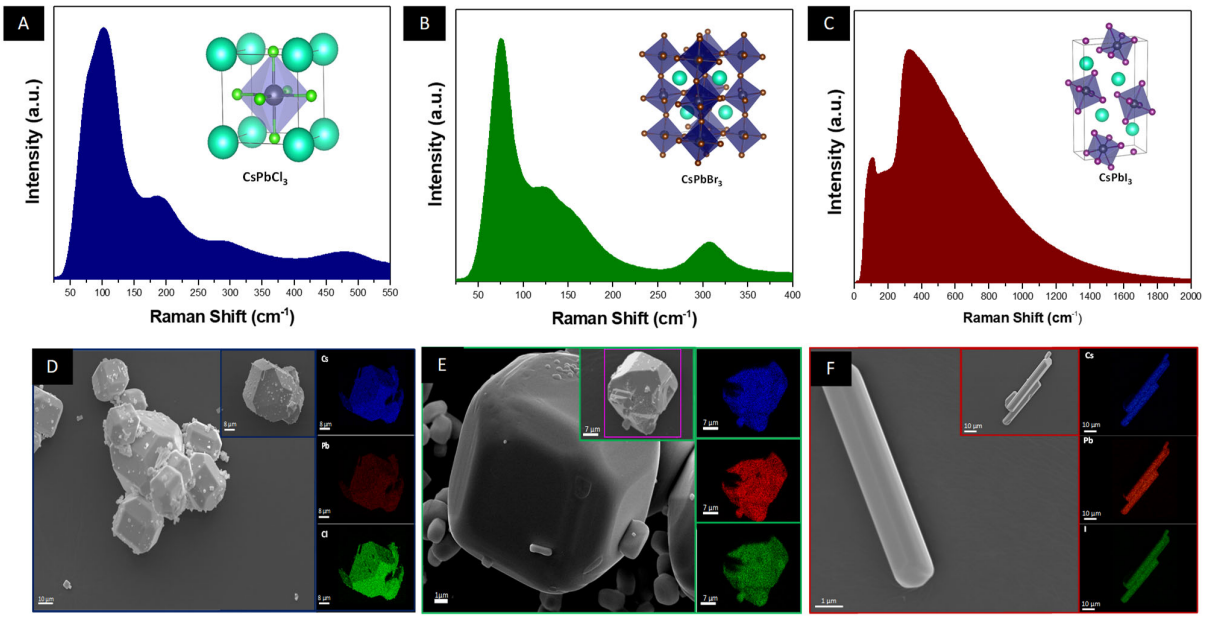

Figure 1. (**A**–**C**) Micro-Raman spectra, (**D**–**F**) SEM images, and EDXS mapping of the $CsPbX_3$ powders synthesized using hydrothermal method at 140 °C: (left) $CsPbCl_3$, (middle) $CsPbBr_3$, and (right) d-$CsPbI_3$. Inset schematic representation of the cubic and orthorhombic unit cells corresponding to the $CsPbX_3$ crystals.

The SEM images in Figure 1D–F show the synthesis route produces for both $CsPbCl_3$ and $CsPbBr_3$, with two different morphologies (ranging from cube to octahedral-like), while $CsPbI_3$ exhibited a uniform morphology, only microrod-like. Energy-dispersive X-ray spectroscopy (EDXS) mapping revealed a similar profile for all samples, indicating that the products contained only Cs, Pb, and X (X = Cl, Br, and I) and were uniformly distributed in the desired compositional atomic percentage as synthesized (Figure 1D–F). However, a comparison between the micro-Raman spectra obtained for these as-prepared samples yielded a distinct characteristic for the $CsPbI_3$ crystals. The peculiar $CsPbI_3$ morphology and the different Raman spectrum compared to $CsPbCl_3$ and $CsPbBr_3$ highlights a higher density of structural defects.

To investigate the optical properties of the crystalline perovskite, a comparison between the projected density of states (DOS) and Tauc plot of the $CsPbX_3$ powders are presented (Figure 2A–C). From the combination of experimental and theoretical approaches, we elucidated the bandgap nature of these materials. Our electronic structure calculations showed that the cubic $CsPbCl_3$ and orthorhombic $CsPbBr_3$ phases have a direct bandgap, while the orthorhombic $CsPbI_3$ structure has an indirect transition. Thus, the experimental bandgap values for the as-synthesized $CsPbX_3$ crystals were calculated from the Tauc plot as 2.60 eV, 2.14 eV, and 2.56 eV for $CsPbCl_3$, $CsPbBr_3$ and $CsPbI_3$, respectively. Hence, this trend is in good agreement with the literature and confirms the formation of δ-$CsPbI_3$ [18,45–49]. These bandgap energy values are strongly dependent on the crystalline perovskite structure. It is well known that, among all-inorganic perovskite materials, the cubic $CsPbI_3$ structure (black phase) as an n-type semiconductor has a suitable bandgap of about 1.70 eV for photovoltaic applications [12,50–53]. However, due to small Cs^+ cation, the cubic $CsPbI_3$ structure is metastable at temperatures below 320 °C [12,51–53]. As a general strategy, researchers have partially replaced Cs^+ with some larger cations, such as methylammonium (abbreviated as MA^+) [54,55] and formamidinium (abbreviated as FA^+) [53,54,56,57]. Hence, stabilizing the cubic $CsPbI_3$ structure in hydrothermal treatment conditions is still challenging and represents an open field of investigation.

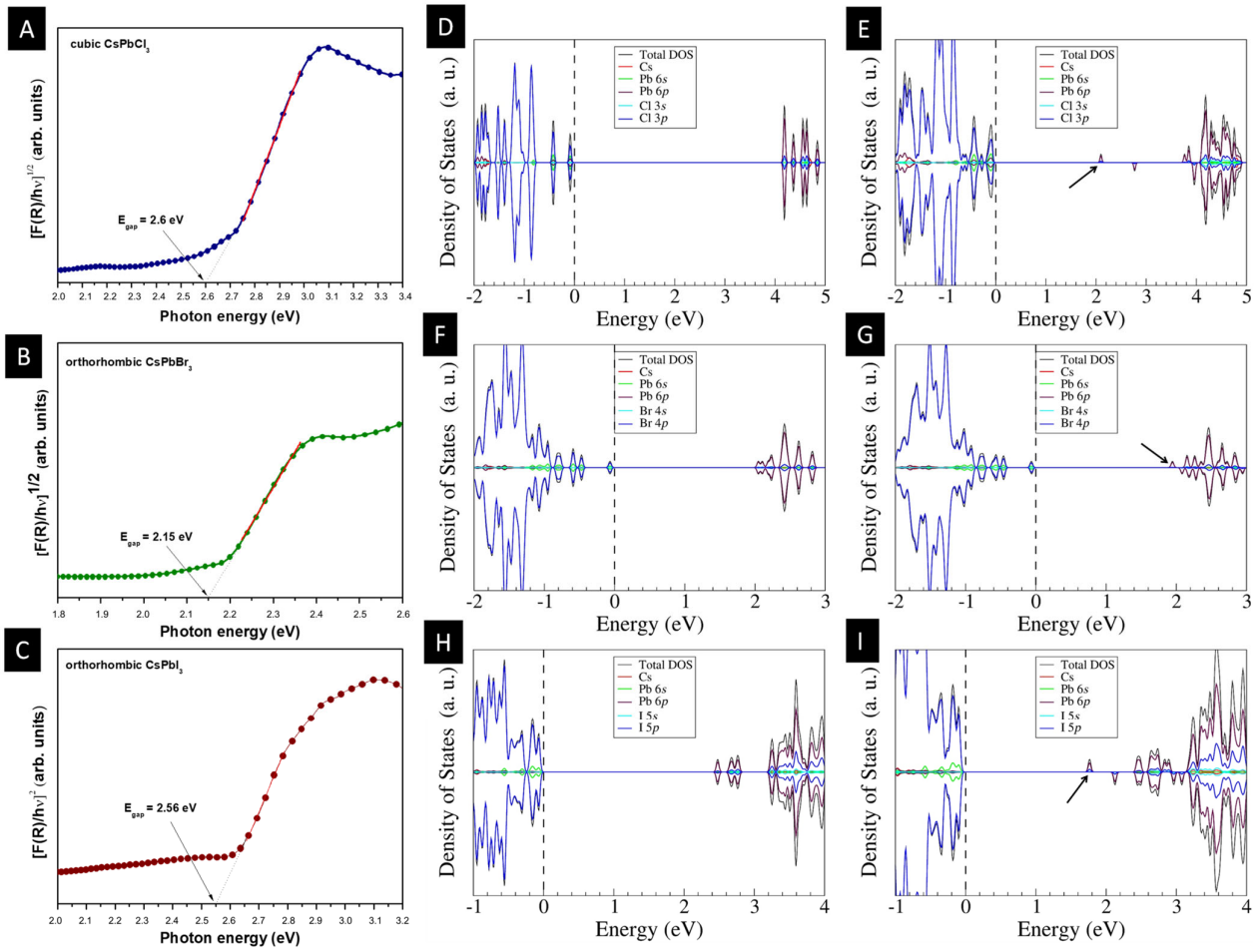

Figure 2. Tauc plot from UV/Vis spectra of the prepared $CsPbX_3$ powders: (**A**) $CsPbCl_3$, (**B**) $CsPbBr_3$, and (**C**) δ-$CsPbI_3$. (**D**–**I**) Projected DOS for the ordered (left) and disordered (right) $CsPbX_3$ models. The position of the defect states is indicated by arrows.

In addition, in order to investigate the influence of defects on the fundamental properties of these crystals, DFT calculations were performed. For this purpose, we removed one anion from the DFT supercell, either Cl, Br, or I, leading to a vacancy concentration of approximately 1%. As expected, the projected DOS (Figure 2D–I) exhibited a vacancy state within the bandgap. This localized state has a p-like character provided that the released electron is occupying one of the partially filled Pb 6*p* orbitals around the vacancy.

The effective masses of the bulk compounds were obtained as the following mean values: $m_e = \Sigma_i m_{e,i}/3$ and $m_h = \Sigma_i m_{h,i}/3$, where I = x, y, and z are correspond to the cartesian directions in the reciprocal space [58]. To estimate $m_{e,i}$ and $m_{h,i}$, we calculated the electronic energies at 13 k points in the vicinity of the bandgap, and fit them to the parabola $E(k) = E_g + \hbar^2k^2(m_0/m)/(2m_0)$, where E_g is the bandgap, m_0 is the electron mass, and m is the effective mass. From the dispersion band structure, we also estimated the effective masses of carriers and the resulting reduced masses $\mu = m_e \times m_h/(m_e + m_h)$ (see Table 1), which can be accessed experimentally [1], thereby serving as a reference to positively evaluate the theoretical level employed here [59,60]. In addition, m_e and m_h for mixed-halide $CsPb(I_{1-x}Br_x)_3$ and $CsPb(Br_{1-x}Cl_x)_3$ perovskites in the orthorhombic phase are also reported in the literature [61].

Table 1. Effective and reduced masses calculated for $CsPbX_3$ structures.

Model	m_e	m_h	μ
$CsPbCl_3$	0.28	0.27	0.14
$CsPbBr_3$	0.24	0.25	0.12
$CsPbI_3$	1.32	1.48	0.70

Lastly, the electrical response of the prepared $CsPbX_3$ pellets as n-type semiconductors was investigated in different humidity conditions at room temperature, as summarized in Figure 3. For this analysis, an impedance spectroscopy (IS) analysis was carried out directly on the $CsPbX_3$ pellets, fitted with an equivalent circuit (Figure 3B,C). The proposed equivalent circuit consists of a contact resistance (denoted as R_S), connected in series with the elements representing the processes in the polycrystalline perovskite: the parallel combination of the charge transport resistance (denoted as R_{tr}) and dielectric capacitance (denoted as C_d). An interesting feature is that, at room temperature, a decrease in the transport resistance could be observed when the samples were exposed to humidity (see Figure 3B). These results are consistent with the literature [62]. However, a more significant variation could be observed for the CsPbI3 pellet. We believe that this is associated with its different morphology observed in SEM analysis. In other words, it suggests that the prepared $CsPbI_3$ pellets had a higher porosity, when compared to $CsPbCl_3$ and $CsPbBr_3$ samples, which could in principle allow a better mobility for water ions or ease the formation of hydrated phases. Therefore, this contributed to higher resistance in the $CsPbI_3$ pellet. Our analysis also demonstrated that the dielectric capacities of these pellets remained practically constant between the different humidity conditions (dry and wet, see Figure 3C), which may support intrinsic electronic polarization effects for these samples [62,63].

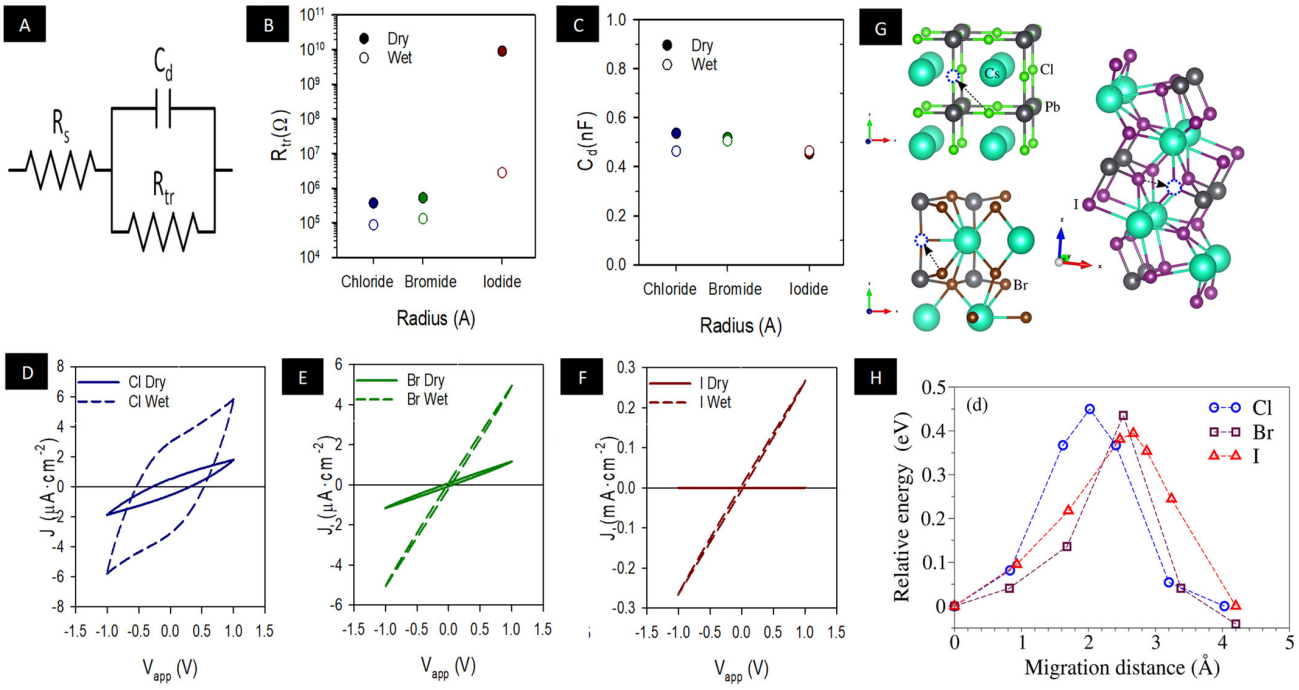

Figure 3. (**B**) Resistance and (**C**) capacitance corresponding to the fitting of the IS measurements with the (**A**) equivalent circuit, and (**D**–**F**) cyclic voltammetry at a rate of 20 mV/s, obtained for dry and wet prepared $CsPbX_3$ pellets at room temperature. (**G**) Migration paths in $CsPbCl_3$, $CsPbBr_3$, and $CsPbI_3$ perovskites and (**H**) corresponding energy profiles along these paths. Vacancies are indicated as blue dotted circles.

From the cyclic voltammetry (see Figure 3D–F), we found an increase in hysteresis with the decrease in monovalent halide radius (i.e., X = Cl, Br and I). For a full description

of this behavior, we performed DFT calculations upon diffusion barriers as present in $CsPbX_3$ bulk structures. We considered the vacancy-mediated migration of halide ions along a direction relevant to the overall diffusion flow, and generated the potential barriers as shown in Figure 3G,H.

On the basis of our DFT calculations, the diffusion barriers for $CsPbCl_3$, $CsPbBr_3$, and $CsPbI_3$ were 0.45, 0.44, and 0.39 eV, respectively [64–66]. The decrease in barrier height for ion migration was likely due to a progressive reduction in the orbital overlap, strongly dependent on the crystal structure. Due to the complex nature of inhomogeneity in $CsPbX_3$ structures, the observed experimental trend can be explained, in principle, by the mechanism of vacancy-mediated anion diffusion, which has been studied for lead halide perovskite materials [64].

4. Conclusions

In summary, the hydrothermal method was developed to prepare $CsPbX_3$ powders at 140 °C for 120 min, highlighting its potential to obtain single-phase perovskite materials at low temperatures with a high reaction yield; this can be considered a very attractive strategy for their obtention on a large scale. Thus, given the wide versatility of these halide perovskite-based materials, the understanding of the structural/electronic differences observed for these materials was analyzed from periodic models based on DFT calculations. The analysis of theoretical results indicated that a breaking symmetry process in these structures is, in principle, strongly associated by order-disorder effects; furthermore, this disordered structure leads to the formation of new electronic states in the bandgap. Our findings also suggest that defect states, in turn, play a pivotal role in the optical and electronic responses of $CsPbX_3$ perovskite structures. Therefore, the combined use of such strategies based on the synergy between theory and practice might provide clues to obtain novel advanced materials that will give rise to new technological applications in the future.

Supplementary Materials: The following supporting information can be downloaded at: https://www.mdpi.com/article/10.3390/nanomanufacturing3020013/s1, Figure S1: XRD patterns of $CsPbX_3$ samples prepared by hydrothermal method: (A) $CsPbCl_3$, (B) $CsPbBr_3$ and (C) $CsPbI_3$.

Author Contributions: Conceptualization, F.A.L.P.; methodology, F.A.L.P., A.O.A., S.M. and C.E.-A.; software, C.E.-A.; validation, F.A.L.P., A.O.A., S.M. and C.E.-A.; formal analysis, F.A.L.P. and S.M.; investigation, F.A.L.P., A.O.A., S.M. and C.E.-A.; resources, F.A.L.P. and F.F.-S.; data curation, F.A.L.P., A.O.A., S.M. and C.E.-A.; writing—original draft preparation, F.A.L.P., C.E.-A. and S.M.; writing—review and editing, F.A.L.P., S.M. and F.F.-S.; visualization, F.A.L.P., A.O.A., S.M. and C.E.-A.; funding acquisition; F.A.L.P. and F.F.-S. All authors have read and agreed to the published version of the manuscript.

Funding: This work was supported by the Brazilian agencies Fundação Araucária, CAPES, and CNPq (203012/2017-8). The MAESTRO project that resulted in this publication received funding from the European Union's Horizon 2020 research and innovation program under grant agreement No. 764787.

Data Availability Statement: The raw data supporting the conclusions of this article will be made available by the authors on request..

Acknowledgments: F.A.L.P. is thankful to CNPq for the fellowships. The authors are especially grateful to Iván Mora Seró (INAM at University Jaume I) for the support and discussion of these results.

Conflicts of Interest: The authors declare no conflict of interest.

References

1. Brenner, T.M.; Egger, D.A.; Kronik, L.; Hodes, G.; Cahen, D. Hybrid organic—Inorganic perovskites: Low-cost semiconductors with intriguing charge-transport properties. *Nat. Rev. Mater.* **2016**, *1*, 15007. [CrossRef]
2. Protesescu, L.; Yakunin, S.; Bodnarchuk, M.I.; Krieg, F.; Caputo, R.; Hendon, C.H.; Yang, R.X.; Walsh, A.; Kovalenko, M.V. Nanocrystals of cesium lead halide perovskites ($CsPbX_3$, X = Cl, Br, and I): Novel optoelectronic materials showing bright emission with wide color gamut. *Nano Lett.* **2015**, *15*, 3692–3696. [CrossRef] [PubMed]
3. Manser, J.S.; Christians, J.A.; Kamat, P.V. Intriguing Optoelectronic Properties of Metal Halide Perovskites. *Chem. Rev.* **2016**, *116*, 12956–13008. [CrossRef]

4. Pinto, F.M.; Dey, S.; Duarte, T.M.; Taft, C.A.; La Porta, F.A. Perovskite-like quantum dots designed for advanced optoelectronic applications. In *Functional Properties of Advanced Engineering Materials and Biomolecules*; La Porta, F., Taft, C., Eds.; Springer: Cham, Switzerland, 2021. [CrossRef]
5. Glazer, A.M. The classification of tilted octahedra in perovskites. *Acta Crystallogr. Sect. B* **1972**, *28*, 3384–3392. [CrossRef]
6. Nakata, M.M.; Mazzo, T.M.; Casali, G.P.; La Porta, F.A.; Longo, E. A large red-shift in the photoluminescence emission of $Mg_1-xSrxTiO_3$. *Chem. Phys. Lett.* **2015**, *622*, 9–14. [CrossRef]
7. Sutton, R.J.; Filip, M.R.; Haghighirad, A.A.; Sakai, N.; Wenger, B.; Giustino, F.; Snaith, H.J. Cubic or Orthorhombic? Revealing the Crystal Structure of Metastable Black-Phase $CsPbI_3$ by Theory and Experiment. *ACS Energy Lett.* **2018**, *3*, 1787–1794. [CrossRef]
8. Goldschmidt, V.M. Die Gesetze der Krystallochemie. *Naturwissenschaften* **1926**, *14*, 477–485. [CrossRef]
9. Akkerman, Q.A.; Abdelhady, A.L.; Manna, L. Zero-Dimensional Cesium Lead Halides: History, Properties, and Challenges. *J. Phys. Chem. Lett.* **2018**, *9*, 2326–2337. [CrossRef]
10. Best Research-Cell Efficiency Chart. Available online: https://www.nrel.gov/pv/cell-efficiency.html (accessed on 15 January 2022).
11. Saliba, M.; Matsui, T.; Domanski, K.; Correa-Baena, J.-P.; Nazeeruddin, M.K.; Zakeeruddin, S.M.; Tress, W.; Abate, A.; Hagfeldt, A.; Gratzel, M. Cesium-containing triple cation perovskite solar cells: Improved stability, reproducibility and high efficiency. *Energy Environ. Sci.* **2016**, *9*, 1989–1997. [CrossRef]
12. Pinto, F.M.; de Conti, M.C.M.D.; Dey, S.; Velilla, E.; Taft, C.A.; La Porta, F.A. Emerging Metal-Halide Perovskite Materials for Enhanced Solar Cells and Light-Emitting Applications. In *Research Topics in Bioactivity, Environment and Energy*; Engineering Materials; Taft, C.A., de Lazaro, S.R., Eds.; Springer: Cham, Switzerland, 2022; pp. 45–85.
13. Jacak, J.E.; Jacak, W.A. Routes for Metallization of Perovskite Solar Cells. *Materials* **2022**, *15*, 2254–2279. [CrossRef]
14. Laska, M.; Krzemińska, Z.; Kluczk-Korch, K.; Schaadt, D.; Popko, E.; Jacak, W.A.; Jacak, J.E. Metallization of solar cells, exciton channel of plasmon photovoltaic effect in perovskite cells. *Nano Energy* **2020**, *75*, 104751. [CrossRef]
15. Gao, Y.; Wu, Y.; Lu, H.; Chen, C.; Liu, Y.; Bai, X.; Yang, L.; Yu, W.W.; Dai, Q.; Zhang, Y. $CsPbBr_3$ perovskite nanoparticles as additive for environmentally stable perovskite solar cells with 20.46% efficiency. *Nano Energy* **2019**, *59*, 517–526. [CrossRef]
16. Thanh, N.T.K.; Maclean, N.; Mahiddine, S. Mechanisms of Nucleation and Growth of Nanoparticles in Solution. *Chem. Rev.* **2014**, *114*, 7610–7630. [CrossRef] [PubMed]
17. Akkerman, Q.A.; Rainò, G.; Kovalenko, M.V.; Manna, L. Genesis, challenges and opportunities for colloidal lead halide perovskite nanocrystals. *Nat. Mater.* **2018**, *17*, 394–405. [CrossRef]
18. Krieg, F.; Ochsenbein, S.; Yakunin, S.; Brinck, S.; Aellen, P.; Süess, A.; Clerc, B.; Guggisberg, D.; Nazarenko, O.; Shynkarenko, Y.; et al. Colloidal $CsPbX_3$ (X = Cl, Br, I) Nanocrystals 2.0: Zwitterionic Capping Ligands for Improved Durability and Stability. *ACS Energy Lett.* **2018**, *3*, 641–646. [CrossRef]
19. Wang, P.; Zhang, X.; Zhou, Y.; Jiang, Q.; Ye, Q.; Chu, Z.; Li, X.; Yang, X.; Yin, Z.; You, J. Solvent-controlled growth of inorganic perovskite films in dry environment for efficient and stable solar cells. *Nat. Comm.* **2018**, *9*, 2225. [CrossRef]
20. Protesescu, L.; Yakunin, S.; Nazarenko, O.; Dirin, D.N.; Kovalenko, M.V. Low-Cost Synthesis of Highly Luminescent Colloidal Lead Halide Perovskite Nanocrystals by Wet Ball Milling. *ACS Appl. Nano Mater.* **2018**, *1*, 1300–1308. [CrossRef] [PubMed]
21. Zhang, J.; Fan, L.; Li, J.; Liu, X.; Wang, R.; Wang, L.; Tu, G. Growth mechanism of $CsPbBr_3$ perovskite nanocrystals by a co-precipitation method in a CSTR system. *Nano Res.* **2019**, *12*, 121–127. [CrossRef]
22. Stoumpos, C.C.; Malliakas, C.D.; Peters, J.A.; Liu, Z.F.; Sebastian, M.; Im, J.; Chasapis, T.C.; Wibowo, A.C.; Chung, D.Y.; Freeman, A.J.; et al. Crystal Growth of the Perovskite Semiconductor $CsPbBr_3$: A New Material for High-Energy Radiation Detection. *Cryst. Growth Des.* **2013**, *13*, 2722–2727. [CrossRef]
23. Kerner, R.A.; Zhao, L.; Xiao, Z.; Rand, B.P. Ultrasmooth metal halide perovskite thin films via sol–gel processing. *J. Mater. Chem. A* **2016**, *4*, 8308–8315. [CrossRef]
24. Liang, J.; Wang, C.; Zhao, P.; Lu, Z.; Xu, Z.; Wang, Y.; Zhu, H.; Hu, Y.; Zhu, G.; Ma, L.; et al. Solution synthesis and phase control of inorganic perovskites for high-performance optoelectronic devices. *Nanoscale* **2017**, *9*, 11841. [CrossRef] [PubMed]
25. Vidyasagar, C.C.; Muñoz Flores, B.M.; Jiménez Pérez, V.M. Recent Advances in Synthesis and Properties of Hybrid Halide Perovskites for Photovoltaics. *Nano-Micro Lett.* **2018**, *10*, 68. [CrossRef] [PubMed]
26. Darr, J.A.; Zhang, J.; Makwana, N.M.; Weng, X. Continuous Hydrothermal Synthesis of Inorganic Nanoparticles: Applications and Future Directions. *Chem. Rev.* **2017**, *117*, 11125–11238. [CrossRef]
27. Kayalvizhi, T.; Sathaya, A.; Preethi Meher, K.R.S. Hydrothermal Synthesis of Perovskite $CsPbBr_3$: Spotlight on the Role of Stoichiometry in Phase Formation Mechanism. *J. Electron. Mater.* **2022**, *51*, 3466–3475. [CrossRef]
28. Kayalvizhi, T.; Sathaya, A.; Preethi Meher, K.R.S. Facile synthesis of monoclinic $CsPbBr_3$—For promising photovoltaic characteristics. *AIP Conf. Proc.* **2020**, *2265*, 030654.
29. La Porta, F.A.; Masi, S. Solvent-Mediated Structural Evolution Mechanism from Cs_4PbBr_6 to $CsPbBr_3$ Crystals. *Nanomanufacturing* **2021**, *1*, 67–74. [CrossRef]
30. Qiu, L.; Ono, L.K.; Qi, Y. Advances and challenges to the commercialization of organic-inorganic halide perovskite solar cell technology. *Mater. Today Energy* **2018**, *7*, 169–189. [CrossRef]
31. Bibi, A.; Lee, I.; Nah, Y.; Allam, O.; Kim, H.; Quan, L.N.; Tang, J.; Walsh, A.; Jang, S.S.; Sargent, E.H.; et al. Lead-free halide double perovskites: Toward stable and sustainable optoelectronic devices. *Mater. Today* **2021**, *49*, 123–144. [CrossRef]
32. Palazon, F.; El Ajjouri, Y.; Sebastia-Luna, P.; Lauciello, S.; Manna, L.; Bolink, H.J. Mechanochemical synthesis of inorganic halide perovskites: Evolution of phase-purity, morphology, and photoluminescence. *J. Mater. Chem. C* **2019**, *7*, 11406. [CrossRef]

33. Rosales, B.A.; Wei, L.; Vela, J. Synthesis and mixing of complex halide perovskites by solvent-free solid-state methods. *J. Solid State Chem.* **2019**, *271*, 206–215. [CrossRef]
34. Pal, P.; Saha, S.; Banik, A.; Sarkar, A.; Biswas, K. All-Solid-State Mechanochemical Synthesis and Post-Synthetic Transformation of Inorganic Perovskite-type Halides. *Chem. Eur. J.* **2018**, *24*, 1811–1815. [CrossRef] [PubMed]
35. Mertzsch, N. Hydrothermal processes in industry. *ChemTexts* **2020**, *6*, 21. [CrossRef]
36. De Conti, M.C.M.D.; Dey, S.; Pottker, W.E.; La Porta, F.A. An overview into advantages and applications of conventional and unconventional hydro(solvo)thermal approaches for novel advanced materials design. In *ChemRxiv*; Cambridge Open Engage: Cambridge, UK, 2022.
37. Pinto, F.M.; Suzuki, V.Y.; Silva, R.C.; La Porta, F.A. Oxygen defects and surface chemistry of reducible oxides. *Front. Mater.* **2019**, *6*, 260. [CrossRef]
38. Giannozzi, P.; Baroni, S.; Bonini, N.; Calandra, M.; Car, R.; Cavazzoni, C.; Ceresoli, D.; Chiarotti, G.L.; Cococcioni, M.; Dabo, I.; et al. QUANTUM ESPRESSO: A modular and open-source software project for quantum simulations of materials. *J. Phys. Condens. Matter* **2009**, *21*, 395502. [CrossRef] [PubMed]
39. Web Standards and Reference Data for First-Principles Simulations. Available online: http://www.quantum-simulation.org (accessed on 5 May 2019).
40. Hamann, D.R. Optimized norm-conserving Vanderbilt pseudopotentials. *Phys. Rev. B* **2017**, *88*, 085117. [CrossRef]
41. Thesika, K.; Murugan, A.V. Microwave-Enhanced Chemistry at Solid–Liquid Interfaces: Synthesis of All-Inorganic $CsPbX_3$ Nanocrystals and Unveiling the Anion-Induced Evolution of Structural and Optical Properties. *Inorg. Chem.* **2020**, *59*, 6161–6175. [CrossRef]
42. Cha, J.-H.; Han, J.H.; Yin, W.; Park, C.; Park, Y.; Ahn, T.K.; Cho, J.H.; Jung, D.-Y. Photoresponse of $CsPbBr_3$ and Cs_4PbBr_6 Perovskite Single Crystals. *J. Phys. Chem. Lett.* **2017**, *8*, 565–570. [CrossRef]
43. Moller, C.K. Crystal structure and photoconductivity of cesium plumbohalides. *Nature* **1958**, *182*, 143. [CrossRef]
44. Trots, D.M.; Myagkota, S.V. High-Temperature Structural Evolution of Caesium and Rubidium Triiodoplumbates. *J. Phys. Chem. Solids* **2008**, *69*, 2520–2526. [CrossRef]
45. Zhao, X.; Tang, T.; Xie, Q.; Gao, L.; Lu, L.; Tang, Y. First-principles study on the electronic and optical properties of the orthorhombic $CsPbBr_3$ and $CsPbI_3$ with Cmcm space group. *New J. Chem.* **2021**, *45*, 15857–15862. [CrossRef]
46. Liao, M.; Shan, B.; Li, M. In Situ Raman Spectroscopic Studies of Thermal Stability of All-Inorganic Cesium Lead Halide ($CsPbX_3$, X = Cl, Br, I) Perovskite Nanocrystals. *J. Phys. Chem. Lett.* **2019**, *10*, 1217–1225. [CrossRef] [PubMed]
47. Lai, M.; Kong, Q.; Bischak, C.G.; Yu, Y.; Dou, L.; Eaton, S.W.; Ginsberg, N.S.; Yang, P. Structural, optical, and electrical properties of phase-controlled cesium lead iodide nanowires. *Nano Res.* **2017**, *10*, 1107–1114. [CrossRef]
48. Zhang, H.; Liu, X.; Dong, J.; Yu, H.; Zhou, C.; Zhang, B.; Xu, Y.; Jie, W. Centimeter-sized inorganic lead halide perovskite CsPbBr3 crystals grown by an improved solution method. *Cryst. Growth Des.* **2017**, *17*, 6426–6431. [CrossRef]
49. Linaburg, M.R.; McClure, E.T.; Majher, J.D.; Woodward, P.M. Cs1–xRbxPbCl$_3$ and Cs1–xRbxPbBr$_3$ Solid Solutions: Understanding Octahedral Tilting in Lead Halide Perovskites. *Chem. Mater.* **2017**, *29*, 3507–3514. [CrossRef]
50. Xu, S.; Libanori, A.; Luo, G.; Chen, J. Engineering bandgap of $CsPbI_3$ over 1.7 eV with enhanced stability and transport properties. *IScience* **2021**, *24*, 102235. [CrossRef]
51. Chhillar, P.; Dhamaniya, B.P.; Pathak, S.K.; Karak, S. Stabilization of Photoactive γ-$CsPbI_3$ Perovskite Phase by Incorporation of Mg. *ACS Appl. Electron. Mater.* **2022**, *4*, 5368–5378. [CrossRef]
52. Filip, M.R.; Eperon, G.E.; Snaith, H.J.; Giustino, F. Steric Engineering of Metal-Halide Perovskites with Tunable Optical Band Gaps. *Nat. Commun.* **2014**, *5*, 5757. [CrossRef]
53. Masi, S.; Gualdrón-Reyes, A.F.; Mora-Seró, I. Stabilization of Black Perovskite Phase in $FAPbI_3$ and $CsPbI_3$. *ACS Energy Lett.* **2020**, *5*, 1974–1985. [CrossRef]
54. Jeon, N.J.; Noh, J.H.; Yang, W.S.; Kim, Y.C.; Ryu, S.; Seo, J.; Seok, S.I. Compositional Engineering of Perovskite Materials for High-Performance Solar Cells. *Nature* **2015**, *517*, 476–480. [CrossRef]
55. Gong, J.; Guo, P.; Benjamin, S.E.; Gregory Van Patten, P.; Schaller, R.D.; Xu, T. Cation engineering on lead iodide perovskites for stable and high-performance photovoltaic applications. *J. Energy Chem.* **2018**, *27*, 1017–1039. [CrossRef]
56. Li, Z.; Yang, M.; Park, J.-S.; Wei, S.-H.; Berry, J.J.; Zhu, K. Stabilizing Perovskite Structures by Tuning Tolerance Factor: Formation of Formamidinium and Cesium Lead Iodide Solid-State Alloys. *Chem. Mater.* **2016**, *28*, 284–292. [CrossRef]
57. Hao, M.; Bai, Y.; Zeiske, S.; Ren, L.; Liu, J.; Yuan, Y.; Zarrabi, N.; Cheng, N.; Ghasemi, M.; Chen, P.; et al. Ligand-assisted cation-exchange engineering for high-efficiency colloidal Cs1−xFAxPbI3 quantum dot solar cells with reduced phase segregation. *Nat. Energy* **2020**, *5*, 79–88. [CrossRef]
58. Luttinger, J.M.; Kohn, W. Motion of electrons and holes in perturbed periodic fields. *Phys. Rev.* **1955**, *97*, 869. [CrossRef]
59. Kohanoff, J. *Electronic Structure Calculations for Solids and Molecules: Theory and Computational Methods*; Cambridge University Press: Cambridge, UK, 2006.
60. Tanaka, K.; Takahashi, T.; Ban, T.; Kondo, T.; Uchida, K.; Miura, N. Comparative study on the excitons in lead-halide-based perovskite-type crystals CH 3NH 3PbBr 3 $CH_3NH_3PbI_3$. *Solid State Commun.* **2003**, *127*, 619–623. [CrossRef]
61. Ghaithan, H.M.; Alahmed, Z.A.; Qaid, S.M.H.; Aldwayyan, A.S. Density Functional Theory Analysis of Structural, Electronic, and Optical Properties of Mixed-Halide Orthorhombic Inorganic Perovskites. *ACS Omega* **2021**, *6*, 30752–30761. [CrossRef]

62. García-Fernández, A.; Moradi, Z.; Bermúdez-García, J.M.; Sánchez-Andújar, M.; Gimeno, V.A.; Castro-García, S.; Señarís-Rodríguez, M.A.; Mas-Marzá, E.; Garcia-Belmonte, G.; Fabregat-Santiago, F. Effect of Environmental Humidity on the Electrical Properties of Lead Halide Perovskites. *J. Phys. Chem. C* **2019**, *123*, 2011–2018. [CrossRef]
63. Bisquert, J.; Bertoluzzi, L.; Mora-Sero, I.; Garcia-Belmonte, G. Theory of Impedance and Capacitance Spectroscopy of Solar Cells with Dielectric Relaxation, Drift-Diffusion Transport, and Recombination. *J. Phys. Chem. C* **2014**, *118*, 18983–18991. [CrossRef]
64. Walsh, A.; Stranks, S.D. Taking Control of Ion Transport in Halide Perovskite Solar Cells. *ACS Energy Lett.* **2018**, *3*, 1983–1990. [CrossRef]
65. Eames, C.; Frost, J.M.; Barnes, P.R.F.; O'Regan, B.C.; Walsh, A.; Islam, M.S. Ionic transport in hybrid lead iodide perovskite solar cells. *Nat. Comm.* **2015**, *6*, 7497. [CrossRef]
66. Mizusaki, J.; Arai, K.; Fueki, K. Ionic conduction of the perovskite-type halides. *Solid State Ion.* **1983**, *11*, 203–211. [CrossRef]